Nuclear Materials and Energy 25 (2020) 100839

Contents lists available at ScienceDirect

Nuclear Materials and Energy

journal homepage: www.elsevier.com/locate/nme

Experimental verification of X-point potential well formation in unfavorable magnetic field direction

M. Wensing [a,*], H. de Oliveira [a], J. Loizu [a], C. Colandrea [a], O. Février [a], S. Gorno [a], H. Reimerdes [a], C. Theiler [a], A. Smolders [a], B.P. Duval [a], C.K. Tsui [b], M. Wischmeier [c], D. Brida [c], S. Henderson [d], M. Komm [e], the TCV Team [1], the EUROfusion MST1 Team [2]

[a] *École Polytechnique Fédérale de Lausanne (EPFL), Swiss Plasma Center (SPC), CH-1015 Lausanne, Switzerland*
[b] *Center for Energy Research (CER), University of California-San Diego (UCSD), La Jolla, CA 92093, USA*
[c] *Max-Planck-Institut fur Plasmaphysik, 85748 Garching b. Munchen, Germany*
[d] *Culham Sci Ctr, CCFE, Abingdon OX14 3DB, Oxon, United Kingdom of Great Britain and Northern Ireland*
[e] *Institute of Plasma Physics of the CAS, Za Slovankou 3, 182 00 Prague 8, Czech Republic*

ARTICLE INFO

Keywords:
Divertor
Tokamak
Electric potential
Drift effects

ABSTRACT

Recent TCV experiments confirm the predicted formation of an electric potential well, below the magnetic X-point, in configurations with unfavorable B_t field direction (ion ∇B drift away from the divertor), that substantially reshapes the typical divertor $E \times B$ flow pattern. The local charge balance $\nabla \cdot \mathbf{j}$ in the private flux region (PFR) of diverted tokamak plasmas has been previously argued to be dominated by parallel and diamagnetic currents. This hypothesis is tested herein in TCV discharges by comparison with SOLPS-ITER simulations, fully accounting for drifts and currents. Simulated parallel currents correctly capture measured current profile characteristics for both targets and both B_t-directions, whereas those omitting drifts fail. It is shown that the resulting parallel currents dictate the electric fields in the PFR for low temperature (detached divertor) conditions resulting in locally negative electric plasma potential in configurations with unfavorable H-mode access.

1. Introduction

This contribution provides experimental evidence for the recently predicted X-point electric potential well formation in unfavorable B_t direction for H-mode access [1]. The presence of such a potential well may influence strongly the divertor performance for reactor operation with unfavorable H-mode access by substantially reshaping the typical $E \times B$ flow pattern. This is of particular concern to advanced tokamak scenarios such as reverse triangularity plasmas or I-mode operation, but also double null configurations where one of the two X-points has the required direction to exhibit a potential well, for any B_t direction.

In general, the parallel electric field on the open field lines of the scrape-off layer (SOL) is determined by the target sheath boundary condition, charge conservation and the parallel electron momentum balance (here for $Z_{eff} = 1$) [2]

$$E_\parallel = \eta_\parallel j_\parallel - \frac{\nabla_\parallel (n_e T_e)}{e n_e} - 0.71 \frac{\nabla_\parallel T_e}{e}. \quad (1)$$

For sufficiently high temperature ($T_e \gg 2$ eV), the first term in Eq. (1) may often be neglected as the Spitzer resistivity $\eta_\parallel$ scales as $T_e^{-3/2}$ [3]. As pressure gradients are typically weak in attached conditions, integration of Eq. (1) yields an electric potential ϕ in the SOL proportional to T_e, implying $E_\parallel$ directed towards the targets. However, for sufficiently low divertor temperature, the parallel electric field takes the form of a simple Ohm's law $E_\parallel = \eta_\parallel j_\parallel$, with $j_\parallel$ determined from the charge balance $\nabla \cdot \mathbf{j} = 0$ and the sheath boundary condition at the targets. The local charge balance in the divertor has been previously argued (JET [4], DIII-D [5], AUG [3], COMPASS [6]) to be established predominantly by parallel currents and diamagnetic currents. The part of the parallel current closing the diamagnetic current is the so called Pfirsch–Schlüter (PS) current. In [1] we derived an analytic expression for the PS current contribution in the PFR for a simplified divertor geometry (straight divertor leg at tilt angle α with negligible flux

* Corresponding author.
E-mail address: mirko.wensing@epfl.ch (M. Wensing).
[1] See the author list of S. Coda et al. 2019 *Nucl. Fusion* **59** 112023.
[2] See the author list of B. Labit et al. 2019 *Nucl. Fusion* **59** 086020.

https://doi.org/10.1016/j.nme.2020.100839
Received 31 July 2020; Received in revised form 19 October 2020; Accepted 2 November 2020
Available online 6 November 2020

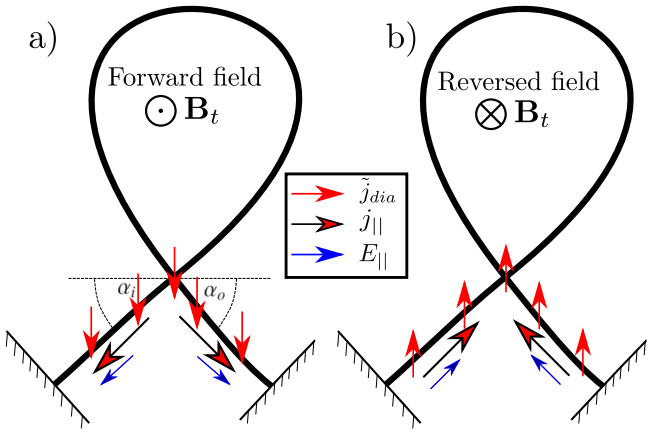

Fig. 1. Schematic flow pattern of PS currents and resulting electric field in the PFR for highly resistive conditions ($E_{\parallel} = \eta_{\parallel} j_{\parallel}$) for (a) forward and (b) reversed B_t direction.

expansion along its extent)

$$j^{PS} = \frac{2p}{B_t^0 R_0} \frac{L_{XP}}{\lambda_j} \left|\frac{B_\theta}{B}\right|_t \cos\alpha. \tag{2}$$

Here $p = n_e T_e + n_i T_i$ denotes the average static pressure along the divertor leg, L_{XP} the poloidal leg length and λ_j the characteristic radial width of the current profile. For a typical lower single null geometry ($cos(\alpha) > 0$, cf. Fig. 1) j^{PS} is defined positive if positive charges flow towards the respective wall, implying that j^{PS} has the same sign, for a given B_t direction in the PFR, at both targets (positive in forward field: $B_t^0 > 0$, negative in reversed field: $B_t^0 < 0$). This results from radial currents related to the grad B and curvature drift, corresponding to the non-divergence-free part of the diamagnetic current $\tilde{j}_{dia}$, into the PFR that are then evacuated along magnetic field lines (cf. Fig. 1). Further contributions to the total current at the target may arise from thermoelectric currents (TE) and currents from external voltage biasing [7]. Thermoelectric contributions are driven by the difference in the electron temperatures T_e at the divertor targets and the accompanied difference in sheath entrance potential, implying an electric current from the hot towards the cold target. TE currents thus appear with opposite sign at the divertor targets. PS- or TE-dominated parallel currents can then be distinguished by measuring the target currents biased to the machine potential, as in [4,6].

In this contribution we demonstrate that TCV divertor currents in the PFR are PS dominated. From Eq. (1), for highly resistive (i.e. detached) divertor conditions the potential near the X-point has to increase/decrease for forward/reversed B_t direction, corresponding to a potential hill/well formation, respectively (cf. Fig. 1). Potential hill formation has been observed in DIII-D experiments and attributed to PS currents and parallel resistivity [5]. Herein, we present, for the first time, experimental evidence for the inverse effect: a potential well structure.

The paper is structured as follows. In Section 2 TCV divertor current measurements are compared with SOLPS-ITER predictions, followed by experimental measurements of the divertor potential in low and high density conditions in Section 3.

2. TCV divertor currents

Recent SOLPS-ITER simulations predict TCV divertor currents in the PFR that are dominated by the PS contribution [1]. This is tested in TCV experiments employing wall-mounted Langmuir probes [8,9] biased to the machine potential, where the strike point is swept across the target, to obtain high spatial and temporal resolution of the resulting current profiles (strike point sweeping period $\tau_{sweep} = 200$ ms, sweeping distance $d_{sweep} = \pm 1$ cm, acquisition frequency $\nu_{LP} = 200$ kHz). We

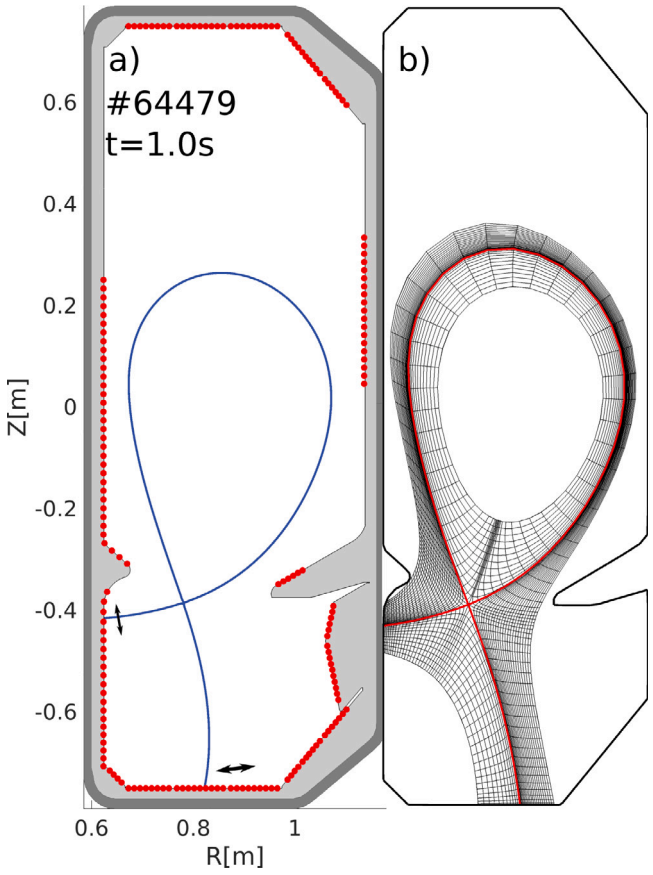

Fig. 2. (a) Discharge geometry and (b) corresponding computational mesh. Wall-mounted Langmuir probes are indicated in red. (For interpretation of the references to color in this figure legend, the reader is referred to the web version of this article.)

investigate the divertor currents in Ohmically heated density ramps (L-mode, $I_p = 190$ kA, $\langle n_e \rangle_l = 3 - 9 \cdot 10^{19}$ m^{-3}, Greenwald fraction $f_{Gw} = 0.25-0.6$) for both B_t directions(Fig. 2a). The upstream density, inferred from Thomson scattering, covers the range $n_e^{sep,omp} = 1 - 2 \cdot 10^{19}$ m^{-3}. For a given line-average density $\langle n_e \rangle_l$, the current profile is mapped upstream, following the LIUQE equilibrium reconstruction [10], and averaged over the sweeping period τ_{sweep}. This method yields a spatially well-resolved target current profile within a density window $\pm 0.5 \cdot 10^{19}$ m^{-3} around the nominal $\langle n_e \rangle_l$. In the following, the current is defined positive if positive charge flows towards the respective target, i.e. in the direction of the ion flow. For PS-dominated currents, one thus expects positive PFR currents on both targets in forward B_t and negative in reversed B_t, c.f. Fig. 1.

Generally, all target currents exhibit a double peaked structure (Figs. 3, 4). In forward B_t direction, the PFR current is positive for both targets, whereas the current flowing in the common flux region (CFR) is positive at the inner and negative at the outer target (Fig. 3a, b). In reversed B_t direction, the PFR current is negative for both targets (ion flow away from the target), the CFR peak is positive but with a significantly lower amplitude w.r.t the PFR peak (Fig. 4a, b). The current amplitude reduction with increasing plasma density is observed for both targets and both field directions. Experimental repeats employing voltage-swept Langmuir probes gave target currents that strongly deviated from ambipolarity with amplitudes comparable to the ion saturation current, i.e. $|j_{\parallel}/j_{\parallel,sat,i}| \sim 1$ (not shown).

Corresponding SOLPS-ITER [11,12] simulations with plasma densities $n_e^{sep,omp} = 1.2 - 3.0 \cdot 10^{19}$ m^{-3}, evaluated at the separatrix at the outer midplane, are obtained by variation of the D_2-gas fueling from a source at the same location as in the experiment, on the vessel

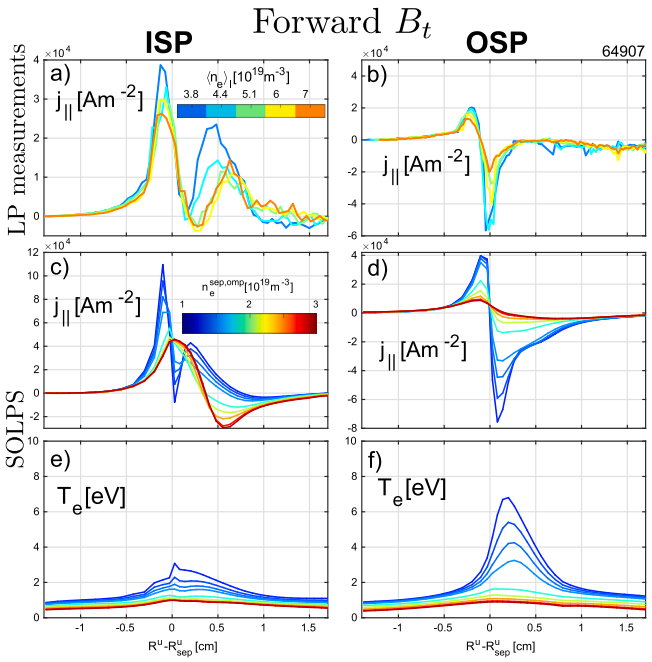

Fig. 3. Parallel currents measured by Langmuir probes for the (a) inner and (b) outer target in forward B_t direction. Both strike points are swept over the target Langmuir probes multiple times during the density ramp. Corresponding simulated target current profiles (c, d) and target temperature profiles (e, f).

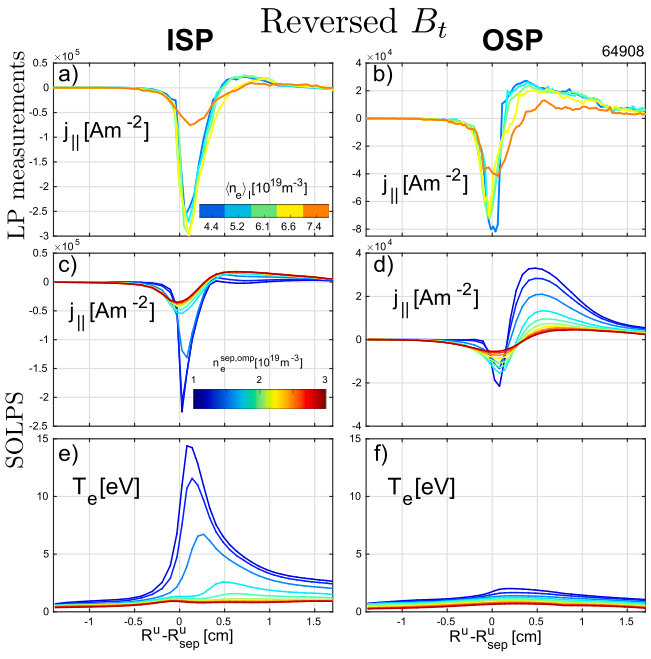

Fig. 4. Parallel currents measured by Langmuir probes for the (a) inner and (b) outer target in reversed B_t direction. Both strike points are swept over the target Langmuir probes multiple times during the density ramp. Corresponding simulated target current profiles (c, d) and target temperature profiles (e, f).

floor at $R = 0.88$ m. An extensive discussion on the parameter settings and implemented reactions used in our TCV simulations is provided in [13, section 2]. Neutrals are treated kinetically by coupling to Eirene. Drifts and current terms are fully included. In absence of a physics model for turbulent cross-field transport, spatially constant anomalous transport coefficients $D_\perp = 0.2\ \mathrm{m}^2/s$ and $\chi_{e,i,\perp} = 1.0\ \mathrm{m}^2/s$ are employed that yield upstream falloff length $\lambda_n \sim 1$ cm, $\lambda_T \sim 0.8$ cm that provide reasonable comparison to upstream plasma profiles inferred from Thomson scattering measurements.

The simulations show remarkable agreement with the characteristic features of the experimental current profiles (Figs. 3c, d and 4c, d). Two peaked target current profiles are observed for all densities, both targets and B_t directions, and the current signs are captured correctly with the sole exception of the high density forward B_t case for the inner target (discussed below). The order of magnitude of target current amplitudes is reasonably well captured by the simulations (deviates up to factor 2–3 in some cases, cf. Fig. 3a, c). The experimentally observed reduction of current amplitude with increasing density is also captured. This reduction is attributed to a decrease in average static pressure $p = n_e T_e + n_i T_i$ along the divertor leg as a detached state is approached that, in turn, reduces the cross-field current $\tilde{j}_r^{dia}$ and hence the PS current according to Eq. (2).

A positive double peak structure for the inner target in forward B_t (Fig. 3 a, c) is only observed for low density simulations. The simulation finds higher target peak temperatures (Figs. 3e, f, 4e, f) at the target in the poloidal $E \times B$ direction, i.e. at the outer/inner target for forward/reversed B_t, respectively, consistent with previous experimental observations [14,15]. At low density, this drives TE currents that appear as a secondary positive peak in the CFR, observed in experiment and simulation (Fig. 3 a,c). The decrease in simulated target temperature on both targets with increasing upstream density leads to a reduction of the TE contribution in the current profile (Fig. 3c). Although, a reduction of the secondary peak with increasing density is, indeed, observed experimentally a transition to negative values is not, indicating that the target temperature asymmetries in the experiment are still sufficient to maintain TE-currents in the CFR, whereas the PFR current is clearly PS-dominated for both targets and both field directions, hence fulfilling the condition for potential well formation (discussed in Section 3).

Simulations with drifts and currents deactivated fail to reproduce the characteristics observed in the experimental profiles. They yield a three peak structure that originates from balancing the parallel and anomalous current $\nabla \cdot (j_{||} + j_{AN}) = 0$, the only remaining terms in the current balance (not shown).

3. X-point potential well formation

A recently installed reciprocating divertor probe array (RDPA) [16] offers unprecedented insight into 2D divertor plasma profiles and is used herein to study the predicted X-point potential well formation. The RDPA probe head harbors 12 independently isolated rooftop Mach probes providing a linear radial resolution of 1 cm and that is reciprocated up to 38 cm vertically through the divertor chamber (Fig. 5a). The probes intercept field lines and separately provide measurements on the flux tube intercepted up- and down-stream. Although the absolute values measured on upstream and downstream probes can vary, the characteristic features presented herein are consistently seen on both.

The probe plasma potential at the sheath entrance ϕ_{se} is inferred from the measured floating potential ϕ_{fl} and the electron temperature via $\phi_{se} = \phi_{fl} + \Lambda T_e$, where $\Lambda = \ln\sqrt{m_i/(2\pi m_e)} \approx 3.16$ for a deuterium plasma. The floating potential ϕ_{fl} corresponds to the potential at which no net current is drawn from the plasma, i.e. electron and ion particle fluxes are equal.

The plasma potential is studied in reversed B_t Ohmic (L-mode, $I_p = 320$ kA) discharges in low and high density plasma conditions ($\langle n_e \rangle_l = 5 \cdot 10^{19}$ m^{-3} and $12 \cdot 10^{19}$ m^{-3}) corresponding to a Greenwald fraction of $f_{Gw} \sim 0.2$ and $f_{Gw} \sim 0.5$. In the low density case the plasma potential is found to be positive, peaked in the CFR, and decaying radially as expected for attached conditions ($\phi \propto T_e$, Fig. 5b). The high density case exhibits a region of negative plasma potential in the vicinity of the separatrix where ϕ_{fl} has decreased more strongly than ΛT_e w.r.t. the low density case (Fig. 5c). In most parts of the common flux region,

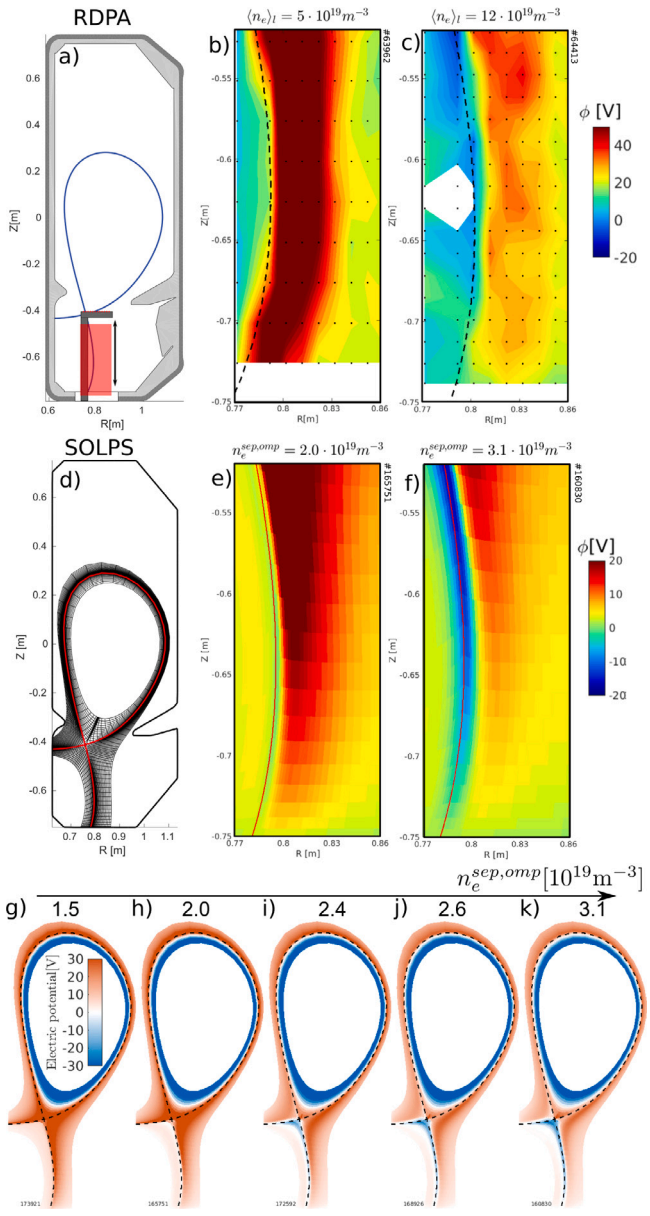

Fig. 5. (a) Plasma shape and RDPA diagnostic with (d) corresponding SOLPS grid. Plasma potential ϕ inferred from RDPA downstream probes in (b) low and (c) high density TCV discharges. Black dots indicate the measurement locations. Corresponding (e) low and (f) high density SOLPS-ITER simulations. (g)–(k) a region of negative electric potential, i.e. the potential well, emerges below the X-point for sufficiently high upstream density (low target temperature).

however, ϕ remains positive. These measurements follow the prediction based on the SOLPS-ITER code [1]. Corresponding SOLPS-ITER simulations (Fig. 5d) at $n_e^{sep,omp} = 2.0 \cdot 10^{19}$ m^{-3} and $3.1 \cdot 10^{19}$ m^{-3} allow direct comparison to the measurements (Fig. 5e, f). The region of negative plasma potential ϕ, Fig. 5f, relates to the simulated X-point potential well structure that emerges continuously during a density scan, Fig. 5g–k. The measured plasma potential drop is consistent with the simulation predictions (~ -10 V). The absolute value differs, however, by a factor ~ 2. Possible experimental reasons for this deviation are inaccuracies in the temperature measurement and possible contributions to Λ by impurities. The TCV simulations, on the other hand, systematically overestimate divertor neutral pressures (factor ~ 3), a discrepancy that is under investigation, and hence yield a more detached divertor state for similar upstream profiles. Nevertheless, these results confirm that the main mechanisms of potential well formation are well captured by the SOLPS-ITER code. The potential well has not been observed in any forward B_t TCV experiments nor discharges with high target temperatures, consistent with the predictions.

4. Conclusions and outlook

The PFR target currents observed in TCV discharges for both B_t directions are consistent with Pfirsch–Schlüter-dominated divertor currents as predicted by the SOLPS-ITER code, and hence are a direct experimental observable of drift effects in the divertor. The characteristics of target current profiles are well captured, whereas the absolute values deviate by up to a factor of 3. The target current amplitude is observed to decrease with increasing plasma density which is attributed to a reduction of the average static pressure in the divertor and the corresponding PS current. TCV's RDPA diagnostic provides unprecedented insight into 2D profiles of the electric potential ϕ in the divertor and provides evidence for the formation of a negative potential well structure in high density reversed B_t conditions in line with the simulation predictions. Potential well formation is not observed in forward B_t discharges nor in attached plasma conditions. Future work will aim at a full comparison of SOLPS-ITER simulations and TCV experiments employing more edge-relevant diagnostics.

CRediT authorship contribution statement

H. de Oliveira: Investigation, Validation. **J. Loizu:** Conceptualization, Methodology. **C. Colandrea:** Investigation. **O. Février:** Investigation, Software, Project administration. **S. Gorno:** Validation. **H. Reimerdes:** Supervision. **C. Theiler:** Supervision. **A. Smolders:** Software. **B.P. Duval:** Supervision. **C.K. Tsui:** Conceptualization. **M. Wischmeier:** Supervision. **D. Brida:** Project administration. **S. Henderson:** Project administration. **M. Komm:** Project administration.

Declaration of competing interest

The authors declare that they have no known competing financial interests or personal relationships that could have appeared to influence the work reported in this paper.

Acknowledgments

This work was carried out within the framework of the EUROfusion Consortium and has received funding from the Euratom research and training programme 2014–2018 and 2019–2020 under Grant Agreement No. 633053. The views and opinions expressed herein do not necessarily reflect those of the European Commission. This work was supported in part by the Swiss National Science Foundation. This work was supported in part by the US Department of Energy under Award Number DE-SC0010529.

References

[1] M. Wensing, et al., Nucl. Fusion 60 (2020) 054005.
[2] F.L. Hinton, Y.B. Kim, Nucl. Fusion 34 (1994) 899.
[3] V. Rozhansky, et al., Contrib. Plasma Phys. 58 (2018) 540–546.
[4] M. Schaffer, et al., J. Nucl. Mater. (2001) 290–293.
[5] A. Jaervinen, et al., Phys. Rev. Lett. 121 (2018) 075001.
[6] C.G. Silva, et al., J. Nucl. Mater. (1999) 266–269.
[7] G.M. Staebler, F.L. Hinton, Nucl. Fusion 29 (1989) 10.
[8] H. De Oliveira, et al., Rev. Sci. Instrum. 90 (2019) 083502.
[9] O. Février, et al., Rev. Sci. Instrum. 89 (2018) 053502.
[10] F. Hofmann, G. Tonetti, Nucl. Fusion 28 (1988) 1871.
[11] S. Wiesen, et al., J. Nucl. Mater. 463 (2015) 480–484.
[12] X. Bonnin, et al., Plasma Fusion Res. 11 (2016) 1403103.
[13] M. Wensing, et al., Plasma Phys. Control. Fusion 61 (2019) 085029.
[14] O. Février, et al., Plasma Phys. Control. Fusion 62 (2020) 035017.
[15] N. Christen, et al., Plasma Phys. Control. Fusion 59 (2017) 105004.
[16] H. de Oliveira, et al., Proceedings of the 46th EPS Conference on Plasma Physics, 2019, P2.1028.